ORNL/TM-2022/1826
CRADA/NFE-19-07545

An Advanced Meso-Scale Peridynamic Modeling Technology using High-Performance Computing for Cost-Effective Product Design and Testing of Carbon Fiber Reinforced Polymer Composites in Light-weight Vehicles

Pablo Seleson
Bo Ren
C.T. Wu
Danielle Zeng
Marco Pasetto

February 2022

CRADA final report for CRADA number NFE-19-07545

Approved for public release. Distribution is unlimited.

OAK RIDGE National Laboratory

ORNL IS MANAGED BY UT-BATTELLE LLC FOR THE US DEPARTMENT OF ENERGY

ORNL/TM-2022/1826
CRADA/NFE-19-07545

Computer Science and Mathematics Division

AN ADVANCED MESO-SCALE PERIDYNAMIC MODELING TECHNOLOGY USING HIGH-PERFORMANCE COMPUTING FOR COST-EFFECTIVE PRODUCT DESIGN AND TESTING OF CARBON FIBER REINFORCED POLYMER COMPOSITES IN LIGHT-WEIGHT VEHICLES

Pablo Seleson
Oak Ridge National Laboratory

Bo Ren
Livermore Software Technology, Ansys

C.T. Wu
Livermore Software Technology, Ansys

Danielle Zeng
Ford Motor Company

Marco Pasetto
University of California San Diego

February 2022

Prepared by
OAK RIDGE NATIONAL LABORATORY
Oak Ridge, TN 37831-6283
managed by
UT-Battelle LLC
for the
US DEPARTMENT OF ENERGY
under contract DE-AC05-00OR22725

CONTENTS

LIST OF FIGURES v
LIST OF TABLES vii
ABBREVIATIONS ix
ACKNOWLEDGMENTS xi
ABSTRACT 1
1. INTRODUCTION 1
2. A PERIDYNAMIC MODEL FOR FAILURE ANALYSIS IN FIBER-REINFORCED COMPOSITE LAMINATES 2
    2.1 BOND-BASED PERIDYNAMICS 2
    2.2 WEAK FORMULATION AND FINITE ELEMENT DISCRETIZATION 2
    2.3 MODELING FIBER REINFORCED COMPOSITE LAMINATES 3
3. TESTS AND RESULTS 6
    3.1 IN-PLANE COUPON TEST ANALYSIS 6
    3.2 OUT-OF-PLANE COUPON TEST ANALYSIS 7
    3.3 COMPONENT CRASH TEST 8
4. SUMMARY 10
5. REFERENCES 11
APPENDIX A. FLEXURAL RIGIDITY OF A FIBER REINFORCED COMPOSITE LAMINATE . . A-1

LIST OF FIGURES

1 Illustration of the peridynamic model of a fiber reinforced composite laminate. 3
2 Tensile coupon test simulation. 6
3 Three-point bending test setting. 7
4 Hat shape three-point bending test: setting & deformed component. 8
5 Hat shape three-point bending test: impactor's velocity & acceleration curves (experimental data provided by Ford Motor Company). 9

LIST OF TABLES

1 Material constants for the in-plane and out-of-plane coupon tests. 6
2 Out-of-plane coupon test: flexural rigidity. 7
3 Material constants for the hat shape three-point bending test. 8

ABBREVIATIONS

CFRP	Carbon fiber reinforced polymer
FEM	Finite element method
FRC	Fiber reinforced composite
HPC	High-performance computing
RVE	Representative volume element

ACKNOWLEDGMENTS

This material is based upon work supported by the US Department of Energy, Office of Energy Efficiency and Renewable Energy (EERE), specifically the Vehicle Technologies Office, High Performance Computing for Materials (HPC4Mtls) program, managed by Lawrence Livermore National Laboratory. This research used resources of the Compute and Data Environment for Science (CADES) at the Oak Ridge National Laboratory, which is supported by the Office of Science of the US Department of Energy under Contract No. DE-AC05-00OR22725. The authors would like to thank Livermore Software Technology, Ansys, for supporting this work by providing an LS-DYNA license to Oak Ridge National Laboratory. The authors would also like to thank Dennis Lam from Ford Motor Company for his helpful discussions on the subject.

ABSTRACT

We study a peridynamic composite modeling technology based on the discontinuous Galerkin finite element method, implemented in the commercial LS-DYNA software, for modeling and prediction of failure in carbon fiber reinforced polymer composites. The proposed technology is developed for the material failure analysis at the meso-scale, which provides the prevailing fiber-matrix interaction mechanism, without adoption of the representative volume element method and thus avoiding complicated numerical calibration procedures. Three types of experimental tests—in-plane coupon test, out-of-plane coupon test, and a component crash test—are simulated in a high-performance computing environment to assess the performance of the proposed peridynamic composite modeling technology.

1. INTRODUCTION

The technical challenges in the current state of the art in numerical modeling of carbon fiber reinforced polymer (CFRP) composites consist of numerical calibration of material constants, simulation of machining/jointing processes, and prediction of crash behavior. In essence, those numerical challenges are strongly related to the inability to analyze material failure problems using the classical homogenization theory in the finite element method (FEM) for CFRP composites. For instance, a numerical assessment of anisotropic material properties for CFRP composites in non-failure analysis can be achieved using the representative volume element (RVE) approach. Various failure models can then be utilized to characterize material damage, including delamination, in constitutive models. In this phenomenological approach, the setting of material constants for the constitutive equations often requires a trial-and-error tuning through experimental validation. This numerical calibration procedure could be strongly problem-dependent and numerically sensitive. Besides this issue, the existing finite element techniques inevitably experience numerical difficulties in modeling material failure in CFRP machining/jointing simulations across different relevant material length scales. Specifically, the continuity assumption in the FEM is inadequate to describe the kinematic discontinuity of displacement fields at the macro-scale for material separation analysis. Compared to the technical challenges in calibrating the material constants and simulating the machining/jointing processes, prediction of crash behavior in CFRP products is even more challenging.

An innovative peridynamic modeling technology for CFRP composites was presented in Ren et al. [2018] and implemented by Livermore Software Technology in the commercial LS-DYNA software, based on the discontinuous Galerkin FEM. This technology was developed for the material failure analysis at the meso-scale, which provides the prevailing fiber-matrix interaction mechanism, without adoption of the RVE method and thus avoiding complicated numerical calibration procedures. Since the proposed meso-scale method considers the decoupling effect between in-plane and delamination failures without element erosion, the simulation of the machining/jointing processes is expected to be very effective and stable. For the same reasons, the proposed meso-scale method is promising for modeling crash behavior in CFRP products. In this report, we present an assessment of the performance of this peridynamic modeling technology through high-performance computing (HPC). Specifically, an in-plane coupon test, an out-of-plane coupon test, and a component crash test are simulated.

This report is organized as follows. In Section 2, we review the bond-based peridynamic theory, the finite element discretization used, and the peridynamic model for fiber reinforced composite (FRC) laminates proposed in Ren et al. [2021], which builds on the modeling technology presented in Ren et al. [2018]. Section 3 describes the tests and reports the corresponding results. A summary is provided in Section 4.

2. A PERIDYNAMIC MODEL FOR FAILURE ANALYSIS IN FIBER-REINFORCED COMPOSITE LAMINATES

2.1 BOND-BASED PERIDYNAMICS

The peridynamic theory is a nonlocal reformulation of the classical theory of continuum mechanics proposed in Silling [2000], which is suitable for modeling material failure and damage due to its lack of differentiability assumption on displacement fields. Given a body $\Omega \subset \mathbb{R}^d$ with d the spatial dimension, the *bond-based* peridynamic equation of motion is given by

$$\rho(\mathbf{x})\frac{\partial^2 \mathbf{u}}{\partial t^2}(\mathbf{x},t) = \int_{\mathcal{H}_\mathbf{x}} \mathbf{f}(\boldsymbol{\eta},\boldsymbol{\xi},t)dV_{\mathbf{x}'} + \mathbf{b}(\mathbf{x},t) \qquad \mathbf{x}\in\Omega, t\geqslant 0, \tag{1}$$

where ρ is the mass density, $\mathbf{u}$ is the displacement field, $\mathbf{b}$ is a prescribed body force density field, and $\mathbf{f}$ is the pairwise force function. We employ the peridynamic notation for a bond $\boldsymbol{\xi} := \mathbf{x}' - \mathbf{x}$ and the relative displacement $\boldsymbol{\eta} := \mathbf{u}(\mathbf{x}',t) - \mathbf{u}(\mathbf{x},t)$. Additionally, we define the peridynamic neighborhood as

$$\mathcal{H}_\mathbf{x} := \{\mathbf{x}' \in \Omega : \|\mathbf{x}' - \mathbf{x}\| \leqslant \delta\},$$

where $\delta > 0$ is the peridynamic horizon. For microelastic materials, each bond has an associated pairwise potential function w such that $\mathbf{f} = \frac{\partial w}{\partial \boldsymbol{\eta}}$. The elastic energy density at $\mathbf{x}\in\Omega$ and $t \geqslant 0$ is given by

$$W(\mathbf{x},t) = \frac{1}{2}\int_{\mathcal{H}_\mathbf{x}} w(\boldsymbol{\eta},\boldsymbol{\xi},t)dV_{\mathbf{x}'}. \tag{2}$$

Equation (1) can model a limited class of materials. Specifically, in the case of isotropy, (1) is restricted to materials with a Poisson's ratio $\nu = 1/4$ in three-dimensional and plane strain settings and $\nu = 1/3$ in two-dimensional and plane stress settings (see Silling [2000], Trageser and Seleson [2020]). To account for arbitrary Poisson's ratios, the generalized *state-based* peridynamic theory has been presented in Silling et al. [2007]. Nevertheless, in this report, we only consider bond-based peridynamic models.

2.2 WEAK FORMULATION AND FINITE ELEMENT DISCRETIZATION

Following Ren et al. [2017], a weak formulation of (1) can be written as

$$\int_\Omega \rho(\mathbf{x})\frac{\partial^2 \mathbf{u}}{\partial t^2}(\mathbf{x},t)\cdot\mathbf{v}(\mathbf{x})dV_\mathbf{x} = \int_\Omega\int_{\mathcal{H}_\mathbf{x}} \mathbf{f}(\boldsymbol{\eta},\boldsymbol{\xi},t)dV_{\mathbf{x}'}\cdot\mathbf{v}(\mathbf{x})dV_\mathbf{x} + \int_\Omega \mathbf{b}(\mathbf{x},t)\cdot\mathbf{v}(\mathbf{x})dV_\mathbf{x}, \tag{3}$$

where $\mathbf{u}\in\mathcal{S}(\Omega)$ and $\mathbf{v}\in\mathcal{S}'(\Omega)$, and the functional spaces are given by

$$\mathcal{S}(\Omega) := \{\mathbf{u}\in L^2(\Omega) | \mathbf{u} = \mathbf{g} \text{ in } \Omega_D\},$$
$$\mathcal{S}'(\Omega) := \{\mathbf{v}\in L^2(\Omega) | \mathbf{v} = \mathbf{0} \text{ in } \Omega_D\},$$

where $\mathbf{g}$ is a function providing displacement boundary conditions in the domain Ω_D. Employing the discontinuous Galerkin finite element discretization for the ith component of (3), we obtain

$$\sum_{g=1}^{n_g}\rho(\mathbf{x}_g)\frac{\partial^2 u_i}{\partial t^2}(\mathbf{x}_g,t)N^B(\mathbf{x}_g)\Delta V_g = \sum_{g=1}^{n_g}\sum_{g'=1}^{n'_g} f_i(\boldsymbol{\eta}_{g,g'},\boldsymbol{\xi}_{g,g'},t)\Delta V_{g'}N^B(\mathbf{x}_g)\Delta V_g + \sum_{g=1}^{n_g} b_i(\mathbf{x}_g,t)N^B(\mathbf{x}_g)\Delta V_g, \quad i=1,2,3,$$

where n_g is the number of Gauss points $\mathbf{x}_g$ in Ω, n'_g is the number of neighbors $\mathbf{x}'_g$ of $\mathbf{x}_g$, N^B is the Bth finite element shape function, $\boldsymbol{\xi}_{g,g'} := \mathbf{x}_{g'} - \mathbf{x}_g$, and $\boldsymbol{\eta}_{g,g'} := \mathbf{u}(\mathbf{x}_{g'},t) - \mathbf{u}(\mathbf{x}_g,t)$.

2.3 MODELING FIBER REINFORCED COMPOSITE LAMINATES

An innovative peridynamic modeling technology for fiber reinforced composite laminates was presented in Ren et al. [2018]. This modeling technology is based on the following assumptions:

1. A laminate is decomposed into two components (see Figure 1a):
   (a) Matrix material: a three-dimensional isotropic bulk material.
   (b) Fiber material: a sequence of transversely isotropic plates immersed in the matrix material.
2. A lamina is simplified as a plane stress transversely isotropic medium with the plane of isotropy perpendicular to the fiber orientation θ (see Figure 1b).
3. Points within a lamina only interact with points in the same lamina and in adjacent laminae (see Figure 1c).
4. A lamina is discretized as a layer of surface elements (see Figure 1c).
5. Peridynamic bonds are classified as *inner-layer* or *inter-layer* bonds (see Figure 1c).

Here, all peridynamic bonds within a lamina are treated equally, and the discretization of a lamina is independent of the fiber orientation.

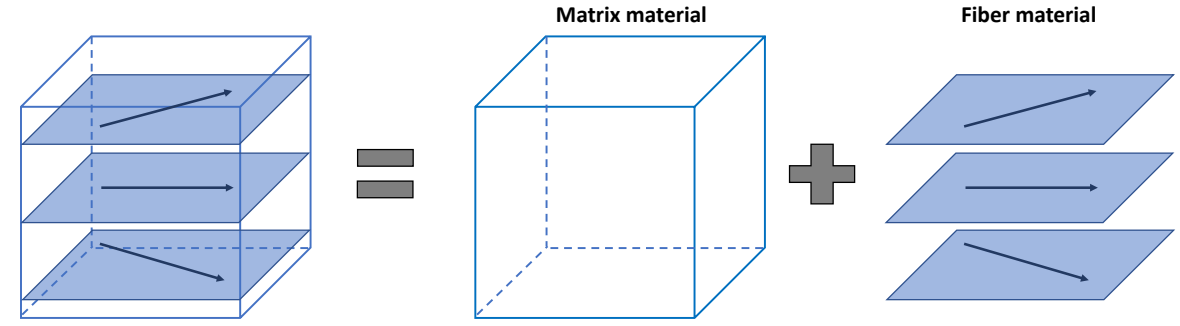

(a) Laminate decomposition into matrix and fiber materials

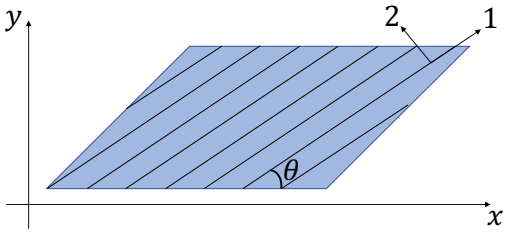

(b) Lamina: transversely isotropic medium

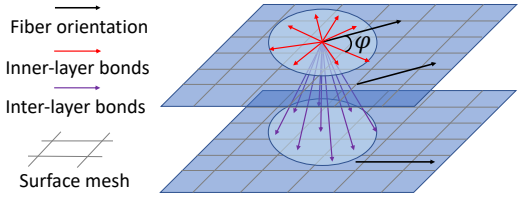

(c) Laminate discretization

Figure 1. Illustration of the peridynamic model of a fiber reinforced composite laminate.

The peridynamic model of a FRC laminate is based on the prototype microelastic brittle peridynamic model (see Silling and Askari [2005]) but extended to incorporate anisotropic behavior, and it is given by

the following pairwise force function:

$$\mathbf{f}(\boldsymbol{\eta}, \boldsymbol{\xi}, t) = \mu(\boldsymbol{\xi}, t) c(\boldsymbol{\xi}) s(\boldsymbol{\eta}, \boldsymbol{\xi}) \frac{\boldsymbol{\xi} + \boldsymbol{\eta}}{\|\boldsymbol{\xi} + \boldsymbol{\eta}\|}, \tag{4}$$

where $c(\boldsymbol{\xi})$ is the bond constant, the bond stretch is defined by

$$s(\boldsymbol{\eta}, \boldsymbol{\xi}) := \frac{\|\boldsymbol{\xi} + \boldsymbol{\eta}\| - \|\boldsymbol{\xi}\|}{\|\boldsymbol{\xi}\|},$$

and $\mu(\boldsymbol{\xi}, t)$ is a history-dependent Boolean-valued function used to model bond breaking, as explained below. The corresponding pairwise potential is

$$w(\boldsymbol{\eta}, \boldsymbol{\xi}, t) = \frac{1}{2} \mu(\boldsymbol{\xi}, t) c(\boldsymbol{\xi}) s^2(\boldsymbol{\eta}, \boldsymbol{\xi}) \|\boldsymbol{\xi}\|. \tag{5}$$

Following the laminate decomposition in Figure 1a, the bond constant is decomposed into isotropic and anisotropic contributions. The bond constant of an inner-layer bond is given by

$$c(\boldsymbol{\xi}) = c^{mt} + c^{fb}(\varphi), \tag{6}$$

where the constant c^{mt} and the function $c^{fb}(\varphi)$ represent the contributions of the matrix material and fiber material, respectively, to the bond response with φ being the relative angle between the bond and the fiber orientation of the lamina (see Figure 1c). To represent the anisotropy of the lamina, $c^{fb}(\varphi)$ is modeled using an 8th-order spherical harmonic expansion following Ghajari et al. [2014]:

$$c^{fb}(\varphi) = A_{00} + A_{20} P_2^0(\cos(\varphi)) + A_{40} P_4^0(\cos(\varphi)) + A_{60} P_6^0(\cos(\varphi)) + A_{80} P_8^0(\cos(\varphi)), \tag{7}$$

where P_n^0, $n = 0, 2, 4, 6, 8$, are associated Legendre polynomials and $A_{00}, A_{20}, A_{40}, A_{60}$, and A_{80} are the corresponding constants. The calibration of the constants is performed using an elastic energy density equivalence between the classical theory of linear elasticity and peridynamics for uniform strain deformations, separately for the matrix material and the fiber material. Specifically, for the matrix material, we calibrate the constant c^{mt} using the classical strain energy density of an isotropic plane stress medium. In contrast, the calibration of the constants $A_{00}, A_{20}, A_{40}, A_{60}$, and A_{80} employs the classical strain energy density of an anisotropic lamina. For further details, see Ren et al. [2021].

The bond constant of an inter-layer bond is given by

$$c(\boldsymbol{\xi}) = c^{mt} + c^{fb}(\varphi, \varphi'), \tag{8}$$

where φ and φ' are the relative angles between the bond and the fiber orientations θ and θ' of the laminae where $\mathbf{x}$ and $\mathbf{x}'$, respectively, are located. The proposed formula for $c^{fb}(\varphi, \varphi')$ is:

$$c^{fb}(\varphi, \varphi') = \frac{c^{fb}(\varphi)\mu_\theta + c^{fb}(\varphi')\mu_{\theta'}}{\mu_\theta + \mu_{\theta'}}, \tag{9}$$

where μ_θ and $\mu_{\theta'}$ are the off-axis shear moduli of each lamina. For further details, see Ren et al. [2021].

In order to model failure, an anisotropic critical stretch criterion for bond breaking is proposed, inspired by the one presented for isotropic materials in Silling and Askari [2005]. The goal of the proposed bond-breaking criteria is to capture mixed failure modes, in particular in-plane failure and delamination. For this purpose, we introduce six empirical failure constants, as follows:

- s_{1t} and s_{1c}: tension and compression, respectively, failure constants for inner-layer bonds along the fiber orientation.
- s_{2t} and s_{2c}: tension and compression, respectively, failure constants for inner-layer bonds perpendicular to the fiber orientation.
- s_{dt} and s_{dc}: tension and compression, respectively, failure constants for inter-layer bonds perpendicular to the fiber orientation.

For inner-layer bonds, the critical bond stretch, $s_0(\varphi)$, is given by

$$s_0(\varphi) = \begin{cases} s_{1t} - 2(s_{1t} - s_{2t})\frac{\varphi}{\pi} & \text{tension,} \\ s_{1c} - 2(s_{1c} - s_{2c})\frac{\varphi}{\pi} & \text{compression,} \end{cases} \tag{10}$$

and, for inter-layer bonds, the critical bond stretch, $s_0(\psi)$ is given by

$$s_0(\psi) = \begin{cases} s_{dt} - 2(s_{dt} - s_{1t})\frac{\psi}{\pi} & \text{tension,} \\ s_{dc} - 2(s_{dc} - s_{1c})\frac{\psi}{\pi} & \text{compression,} \end{cases} \tag{11}$$

where ψ is the angle between the bond and the laminate normal. For further details, see Ren et al. [2021]. A bond breaks (irreversibly) when the condition $s(\boldsymbol{\eta}, \boldsymbol{\xi}) > s_0$ is met, where $s_0 = s_0(\varphi)$ for inner-layer bonds and $s_0 = s_0(\psi)$ for inter-layer bonds. More specifically, $\mu(\boldsymbol{\xi}, t)$ is given by (see Silling and Askari [2005])

$$\mu(\boldsymbol{\xi}, t) = \begin{cases} 1 & s(\tilde{\boldsymbol{\eta}}, \boldsymbol{\xi}) < s_0 \text{ for all times } 0 \leqslant \tilde{t} \leqslant t, \\ 0 & \text{otherwise,} \end{cases} \tag{12}$$

where $\tilde{\boldsymbol{\eta}} := \mathbf{u}(\mathbf{x}', \tilde{t}) - \mathbf{u}(\mathbf{x}, \tilde{t})$.

3. TESTS AND RESULTS

3.1 IN-PLANE COUPON TEST ANALYSIS

We perform tensile coupon test simulations (see illustration in Figure 2a) and compute the *off-axis elastic modulus*, E_θ, of FRC laminates for different fiber orientations. A 2-layer unidirectional laminate is employed with the material constants reported in Table 1, where ρ is the mass density, E_1 and E_2 are the Young's modulus along and perpendicular to the fiber orientation, respectively, ν_{12} is the corresponding Poisson's ratio*, and μ is the shear modulus. The laminate dimensions are 75 mm $\times$ 15 mm $\times$ 0.2 mm, and each lamina is discretized with 75×15 square elements. The peridynamic horizon is selected as $\delta = 1.01\Delta x$, where $\Delta x = 1$ mm is the square element side length. A velocity boundary condition is imposed on the right surface of the laminate, which linearly increases from 0 mm/s to 2 mm/s over the first millisecond and then stays constant at 2 mm/s; the total simulation time is $T = 2.5$ ms. A zero displacement boundary condition along the x-direction is imposed on the left surface of the laminate.

ρ [ton/mm^3]	E_1 [GPa]	E_2 [GPa]	ν_{12}	μ [GPa]
1.65×10^{-9}	135	8.5	0.34	4.8

Table 1. Material constants for the in-plane and out-of-plane coupon tests.

The stress at the right surface of the deformed laminate is computed by $\sigma = \frac{F}{A}$, where F is the total force applied on the nodes at that surface and $A = 15$ mm $\times$ 0.2 mm $= 3$ mm^2 is the area of that surface. The horizontal strain of the deformed laminate is computed by $\varepsilon = \frac{\Delta L}{L}$, where $L = 75$ mm is the length of the laminate and ΔL is the change in that length. The numerical off-axis elastic modulus is then computed by

$$E_\theta^{\text{num}} = \frac{\sigma}{\varepsilon}. \tag{13}$$

We compare numerical results computed with (13) with corresponding analytical values for the off-axis elastic modulus given by (see Reddy [2003]):

$$E_\theta = \frac{E_1}{\cos^4(\theta) + \cos^2(\theta)\sin^2(\theta)\left(-2\nu_{12} + \frac{E_1}{\mu}\right) + \sin^4(\theta)\frac{E_1}{E_2}}, \tag{14}$$

where θ is the fiber orientation. Figure 2b presents a comparison between numerical and analytical values of the off-axis elastic modulus for various fiber orientations. A close match is obtained between the numerical results and the analytical predictions.

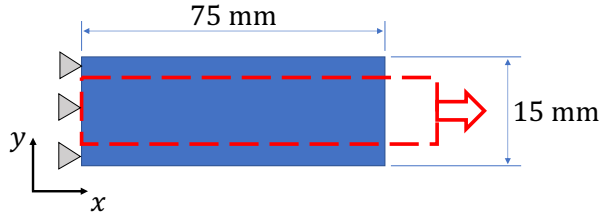

(a) Illustration of the tensile coupon test.

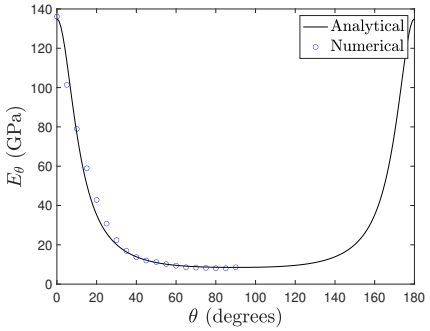

(b) Off-axis elastic modulus profile.

Figure 2. Tensile coupon test simulation.

*The Poisson's ratio ν_{12} is used to decompose the laminae into the matrix and fiber materials (see Ren et al. [2021]).

3.2 OUT-OF-PLANE COUPON TEST ANALYSIS

We perform three-point bending test simulations (see the simulation setting in Figure 3) and compute the *flexural rigidity*, EI_θ, of FRC laminates for different fiber orientations. An 8-layer unidirectional laminate is employed with the material constants reported in Table 1. The laminate dimensions are 125 mm $\times$ 15 mm $\times$ 2 mm, and each lamina is discretized with 50×6 square elements. The peridynamic horizon is selected as $\delta = 1.01\Delta x$, where $\Delta x = 2.5$ mm is the square element side length. The laminate is supported by two cylinders of diameter 4 mm and length 40 mm; the supports are equally distant from the center of the laminate and the distance between their centers is $L = 80$ mm. The impactor is a cylinder of diameter 10 mm and length 40 mm. The impactor's velocity in the negative z-direction linearly increases in magnitude from 0 mm/s to 100 mm/s over the first millisecond and then stays constant at -100 mm/s, and the impactor hits the laminate at the top center; the total simulation time is $T = 25.5$ ms. The supports and the impactor are modeled as rigid bodies, and we employ the rigid wall contact algorithm in LS-DYNA.

The flexural rigidity is computed numerically as follows:

$$EI_\theta^{\text{num}} = \frac{PL^3}{48 w_{L/2}}, \tag{15}$$

where P is the force exerted at the center of the laminate and $w_{L/2}$ is the corresponding displacement; note that $P/w_{L/2}$ is the slope of the corresponding force-displacement curve. We compute this slope using the reaction force and displacement of the impactor. The analytical value of the flexural rigidity, EI_θ, as a function of the fiber orientation, θ, is obtained from Reddy [2003] (see Appendix A). The relative error is computed as follows:

$$\text{Relative Error} = \frac{|EI_\theta^{\text{num}} - EI_\theta|}{EI_\theta}. \tag{16}$$

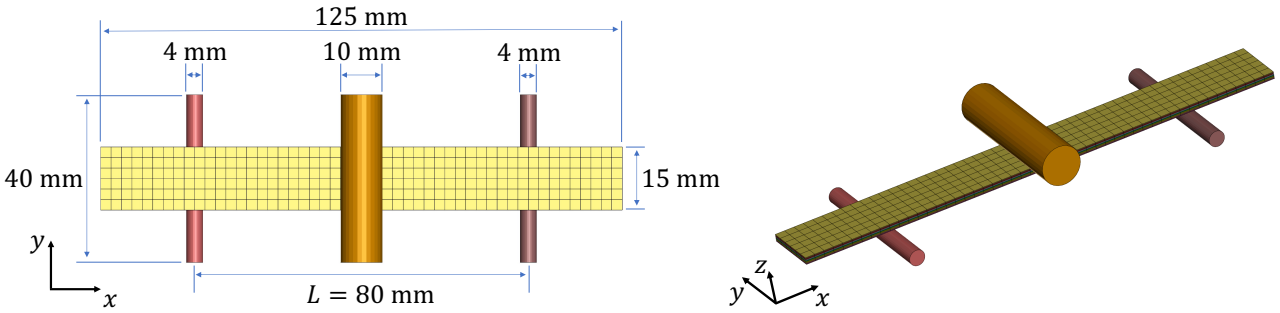

(a) Top view. **(b) 3D view.**

Figure 3. Three-point bending test setting.

Table 2 reports the numerical and analytical values obtained for the flexural rigidity for three fiber orientations, demonstrating that a relatively close match is attained between these values.

θ [degree]	EI_θ [N mm^2]	EI_θ^{num} [N mm^2]	Relative Error [%]
0	1,350,000	1,337,982	0.9
45	121,821	133,760	9.8
90	85,000	89,015	4.7

Table 2. Out-of-plane coupon test: flexural rigidity.

3.3 COMPONENT CRASH TEST

To validate the failure response of the peridynamic model of a FRC laminate, we employ a hat shape three-point bending test (see the simulation setting in Figure 4) and compute the acceleration profile in time. A 24-layer laminate with stacking sequence $[0/60/-60/0/60/-60]_{2S}$ is employed with the material constants reported in Table 3. The hat shape laminate dimensions are indicated in Figures 4a and 4b, and each lamina has a thickness of 0.2 mm. From the 24 laminae, half conform the hat shape base and half the hat shape top part. The base dimensions are 400 mm $\times$ 175.6 mm $\times$ 2.4 mm, and each lamina is discretized with 114×44 square elements. The laminae in the hat shape top part employ the same discretization. The peridynamic horizon is selected as $\delta = 0.8\Delta x$, where $\Delta x = 4.0$ mm is the square element side length. The hat shape laminate is supported by two cylindrical shells of diameter 25 mm, length 186 mm, and thickness 0.1 mm; the supports are equally distant from the center of the hat shape laminate and the distance between their centers is 400 mm (see Figure 4b). The impactor is a cylindrical shell of diameter 100 mm, length 186 mm, and thickness 0.1 mm (see Figure 4b). The supports and the impactor are all modeled as rigid bodies with mass density 4.3647 gr/mm^3 and Young's modulus 391.709 GPa. The impactor has an initial velocity of -4.8 mm/ms and hits the hat shape component at the top center; the resulting velocity profile is shown in Figure 5a. We employ the nodes-to-surface contact algorithm in LS-DYNA. The six empirical failure constants are chosen as $s_{1t} = 0.06$, $s_{1c} = 0.12$, $s_{2t} = 0.035$, $s_{2c} = 0.07$, $s_{dt} = 0.3$, and $s_{dc} = 0.6$.

ρ [gr/mm^3]	E_1 [GPa]	E_2 [GPa]	ν_{12}	μ [GPa]
1.54×10^{-3}	127.8	8.567	0.33	4.85

Table 3. Material constants for the hat shape three-point bending test.

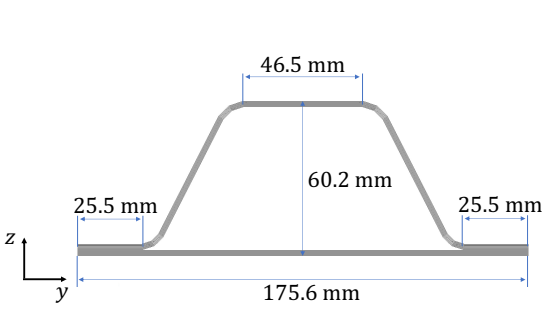

(a) Setting: side view.

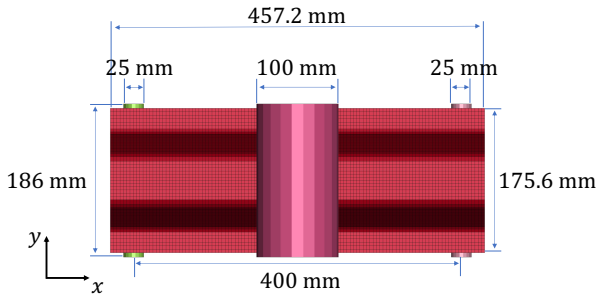

(b) Setting: top view.

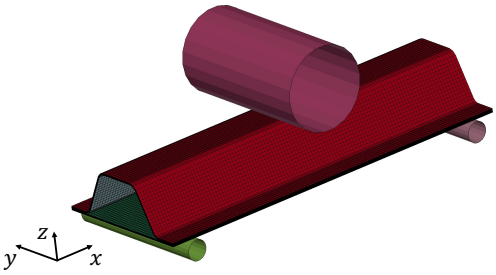

(c) Setting: 3D view.

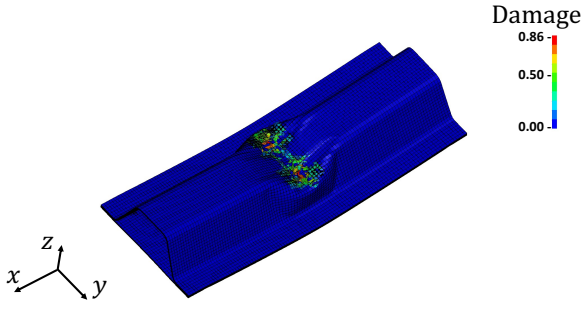

(d) Deformed component: 3D view.

Figure 4. Hat shape three-point bending test: setting & deformed component.

In Figure 4d, we present the deformed structure colored by damage, which includes in-plane and delamination damage (see Ren et al. [2018]). The simulation shows a buckled sidewall as well as a damage zone near the contact area; both phenomena have been observed experimentally (see Zhou et al. [2020]). Finally, Figure 5b reports a comparison of the acceleration profile in time between the simulation and the experimental data provided by Ford Motor Company. The acceleration in the simulation is computed by dividing the reaction force experienced by the impactor by the impactor's mass. The results show a close match between the simulation and the experimental results.

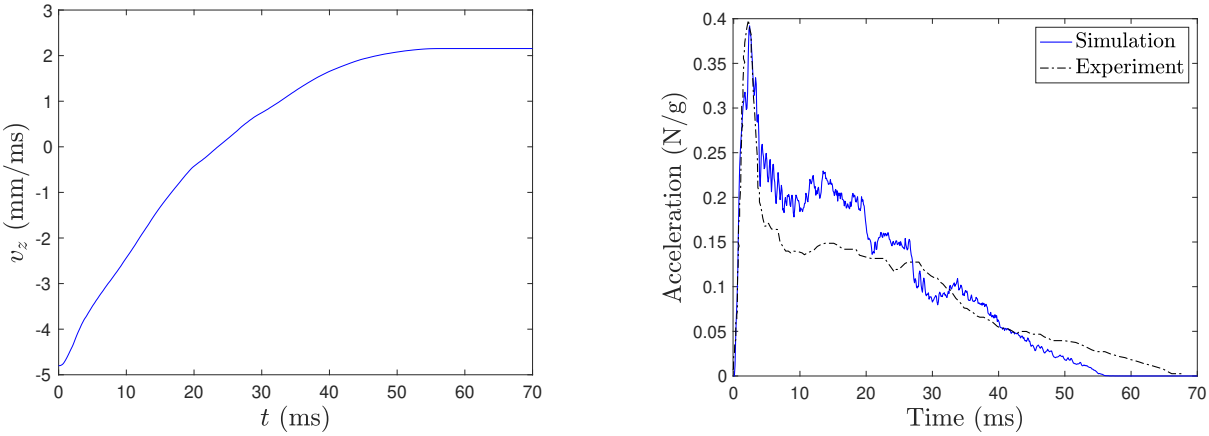

(a) Impactor's velocity. **(b) Acceleration curves.**

Figure 5. Hat shape three-point bending test: impactor's velocity & acceleration curves (experimental data provided by Ford Motor Company).

4. SUMMARY

This report presents validation simulations for a peridynamic model of a FRC laminate proposed in Ren et al. [2021]. We studied the elastic response of the peridynamic model by computing the off-axis elastic modulus with tensile coupon test simulations as well as the flexural rigidity with three-point bending test simulations for different fiber orientations, and we compared simulation results with analytical predictions resulting in a close match between numerical and analytical values. The failure response of the peridynamic model was also investigated using a hat shape three-point bending test simulation and comparing numerical results with experimental data. The investigation included a quantitative comparison of acceleration curves as well as a qualitative assessment of the structural deformation, which included sidewall buckling and damage around the contact area, both resulting in a close match between the simulation and the experiment. While additional studies are recommended to further investigate the sensitivity of numerical results to various components of the peridynamic model, such as the choice of contact algorithm, discretization, horizon, and delamination failure model, overall the results demonstrate that the proposed peridynamic model can serve as an effective tool for the simulation of failure in CFRP composites.

5. REFERENCES

M. Ghajari, L. Iannucci, and P. Curtis. A peridynamic material model for the analysis of dynamic crack propagation in orthotropic media. *Computer Methods in Applied Mechanics and Engineering*, 276: 431–452, 2014.

J. N. Reddy. *Mechanics of Laminated Composite Plates and Shells: Theory and Analysis*. CRC press, 2nd edition, 2003.

B. Ren, C.T. Wu, and E. Askari. A 3D discontinuous Galerkin finite element method with the bond-based peridynamics model for dynamic brittle failure analysis. *International Journal of Impact Engineering*, 99:14–25, 2017.

B. Ren, C.T. Wu, P. Seleson, D. Zeng, and D. Lyu. A peridynamic failure analysis of fiber-reinforced composite laminates using finite element discontinuous Galerkin approximations. *International Journal of Fracture*, 214:49–68, 2018.

B. Ren, C.T. Wu, P. Seleson, D. Zeng, M. Nishi, and M. Pasetto. An FEM-based peridynamic model for failure analysis of unidirectional fiber-feinforced laminates. *Journal of Peridynamics and Nonlocal Modeling*, 2021. https://doi.org/10.1007/s42102-021-00063-0.

S.A. Silling. Reformulation of elasticity theory for discontinuities and long-range forces. *Journal of the Mechanics and Physics of Solids*, 48:175–209, 2000.

S.A. Silling and E. Askari. A meshfree method based on the peridynamic model of solid mechanics. *Computers & Structures*, 83:1526–1535, 2005.

S.A. Silling, M. Epton, O. Weckner, J. Xu, and E. Askari. Peridynamic states and constitutive modeling. *Journal of Elasticity*, 88:151–184, 2007.

J. Trageser and P. Seleson. Bond-based peridynamics: A tale of two Poisson's ratios. *Journal of Peridynamics and Nonlocal Modeling*, 2:278–288, 2020.

G. Zhou, Q. Sun, J. Fenner, D. Li, D. Zeng, X. Su, and Y. Peng. Crushing behaviors of unidirectional carbon fiber reinforced plastic composites under dynamic bending and axial crushing loading. *International Journal of Impact Engineering*, 140:103539, 2020.

APPENDIX A. FLEXURAL RIGIDITY OF A FIBER REINFORCED COMPOSITE LAMINATE

APPENDIX A. FLEXURAL RIGIDITY OF A FIBER REINFORCED COMPOSITE LAMINATE

Assume a fiber reinforced composite laminate of length L, width b, and thickness h (along the z-direction) composed of N laminae arranged in a certain stacking sequence. Each lamina is modeled as an orthotropic medium in plane stress state with the following linear constitutive relation (see Reddy [2003]):

$$\begin{bmatrix} \sigma_1 \\ \sigma_2 \\ \sigma_6 \end{bmatrix} = \begin{bmatrix} Q_{11} & Q_{12} & 0 \\ Q_{12} & Q_{22} & 0 \\ 0 & 0 & Q_{66} \end{bmatrix} \begin{bmatrix} \varepsilon_1 \\ \varepsilon_2 \\ \varepsilon_6 \end{bmatrix}, \tag{17}$$

where, using Voigt notation, σ_1, σ_2, and σ_6 are the components of the stress tensor, $\varepsilon_1, \varepsilon_2$, and ε_6 are the components of the infinitesimal strain tensor, and Q_{11}, Q_{12}, Q_{22}, and Q_{66} are plane stress-reduced stiffnesses given by (see Reddy [2003])

$$Q_{11} = \frac{E_1}{1 - \nu_{12}\nu_{21}}, \quad Q_{12} = \frac{\nu_{12}E_2}{1 - \nu_{12}\nu_{21}}, \quad Q_{22} = \frac{E_2}{1 - \nu_{12}\nu_{21}}, \quad \text{and} \quad Q_{66} = \mu, \tag{18}$$

where E_1 and E_2 are the Young's modulus along and perpendicular to the fiber orientation, respectively, ν_{12} is the corresponding Poisson's ratio, and μ is the shear modulus; note that $\nu_{21} = \nu_{12}\frac{E_2}{E_1}$ (see Reddy [2003]).

In a laminate, each lamina has its material axes oriented possibly in a different orientation with respect to the laminate coordinates. Thus, we apply a transformation to the plane stress-reduced stiffnesses of each lamina. Let θ_k be the orientation of the kth lamina. Then, the transformed plane stress-reduced stiffnesses for the kth lamina are given by (see Reddy [2003])

$$\begin{aligned}
\bar{Q}_{11}^{(k)} &= Q_{11}\cos^4(\theta_k) + 2(Q_{12} + 2Q_{66})\sin^2(\theta_k)\cos^2(\theta_k) + Q_{22}\sin^4(\theta_k), \\
\bar{Q}_{12}^{(k)} &= (Q_{11} + Q_{22} - 4Q_{66})\sin^2(\theta_k)\cos^2(\theta_k) + Q_{12}(\sin^4(\theta_k) + \cos^4(\theta_k)), \\
\bar{Q}_{22}^{(k)} &= Q_{11}\sin^4(\theta_k) + 2(Q_{12} + 2Q_{66})\sin^2(\theta_k)\cos^2(\theta_k) + Q_{22}\cos^4(\theta_k), \\
\bar{Q}_{16}^{(k)} &= (Q_{11} - Q_{12} - 2Q_{66})\sin(\theta_k)\cos^3(\theta_k) + (Q_{12} - Q_{22} + 2Q_{66})\sin^3(\theta_k)\cos(\theta_k), \\
\bar{Q}_{26}^{(k)} &= (Q_{11} - Q_{12} - 2Q_{66})\sin^3(\theta_k)\cos(\theta_k) + (Q_{12} - Q_{22} + 2Q_{66})\sin(\theta_k)\cos^3(\theta_k), \\
\bar{Q}_{66}^{(k)} &= (Q_{11} + Q_{22} - 2Q_{12} - 2Q_{66})\sin^2(\theta_k)\cos^2(\theta_k) + Q_{66}(\sin^4(\theta_k) + \cos^4(\theta_k)).
\end{aligned}$$

The kth lamina with width b and uniform thickness is given by material points with z-coordinates in the range (z_k, z_{k+1}), where $z_k = -h/2 + (k-1)\Delta z$ with $\Delta z = h/N$; note that $z_1 = -h/2$ and $z_{N+1} = h/2$. Then, the elements of the bending stiffness tensor $\mathbf{D}$ are given by (see Reddy [2003])

$$D_{ij} = \frac{1}{3}\sum_{k=1}^{N} \bar{Q}_{ij}^{(k)}(z_{k+1}^3 - z_k^3). \tag{19}$$

Let us consider a unidirectional laminate with orientation θ. In this case, $\bar{Q}_{ij}^{(k)} = \bar{Q}_{ij}$ for all k, and we can simplify (19) as follows:

$$D_{ij} = \frac{1}{3}\bar{Q}_{ij}\sum_{k=1}^{N}(z_{k+1}^3 - z_k^3) = \frac{1}{3}\bar{Q}_{ij}(z_{N+1}^3 - z_1^3) = \frac{h^3}{12}\bar{Q}_{ij}. \tag{20}$$

The corresponding flexural rigidity, EI_θ, is calculated as (see Reddy [2003])

$$EI_\theta = \frac{b}{(\mathbf{D}^{-1})_{11}}, \tag{21}$$

where $\mathbf{D}^{-1}$ is the inverse of the bending stiffness tensor.